North Atlantic wintertime intraseasonal variability and its sensitivity to GCM horizontal resolution

By FRANCISCO J. DOBLAS-REYES[1]*, MICHEL DÉQUÉ, FRANCISCO VALERO[2] and DAVID B. STEPHENSON[1] [1]*Météo-France CNRM, 42 Av. Gaspard Coriolis, 31057 Toulouse Cedex, France; [2]Dpto. Física de la Tierra, Astronomía y Astrofísica II, Universidad Complutense, Ciudad Universitaria, 28040 Madrid, Spain*

ABSTRACT

The wintertime extratropical intraseasonal variability in the North Atlantic-European region has been analysed, and the ability of an atmospheric general circulation model to simulate it at different horizontal resolutions is discussed. Three runs of the French global spectral model (ARPEGE) are investigated: both medium (T42) and high (T106) resolution, and a conformally stretched T63 version with maximum resolution over the Mediterranean. Circulation features are validated against ECMWF analyses. The systematic errors in the simulated variability have been isolated using space-time spectral and complex principal component analyses. The time-mean structure of the 500 hPa geopotential height indicates that the model is too zonal, especially at high resolution, with a stronger than normal synoptic-scale activity. The Atlantic storm track penetrates too far eastward over Europe, is too far south and does not veer to the northeast at the exit of the jet. These features may be in part associated with too strong barotropic forcing of the mean flow by the synoptic-scale eddies on the equatorward side of the jet. Despite the overly strong zonal mean flow, the high resolution simulation has more realistic storm tracks than the other two versions. Low-frequency intraseasonal variance is underestimated at each resolution, mainly north of 50°N. Furthermore, the model lacks planetary-scale slow westward travelling waves and does not show realistic spatial modes of low-frequency variability at any resolution. Blocking frequency is underestimated and the blocking patterns are shifted eastward, following the excess of storm track penetration over Europe. However, these drawbacks are slightly improved at higher (T106) resolution, especially for blocking.

1. Introduction

The most common systematic errors of tropospheric extratropical flow in climate models, regardless of whether they make use of either a grid point or spectral numerical framework, are the excessive zonality of the jet streams and the undersimulation of the time-mean stationary eddies (Tibaldi et al., 1990; Anderson, 1993; Huth, 1994; D'Andrea et al., 1996). However, a complete understanding of the model behaviour requires an explanation not only of the time-mean state but also of the time-varying components. Biases in the model time-mean structure may have a pronounced effect upon the model simulation of transients (Reynolds et al., 1996), which in turn can have a feedback effect on stationary waves. In order to be useful for applications such as climate change simulations or long-range prediction, climate models should simulate the correct mean climate by the correct processes. This study is concerned with validating midlatitude intraseasonal variability, which shows up as a complex interacting set of phenomena, which are, with different degrees, misrepresented in many general

circulation models (Lau and Nath, 1987; Ponater et al., 1994; D'Andrea et al., 1996). Following Ghil and Mo (1991), intraseasonal variability may be defined as variability with time periods less than 90–100 days. Lanzante (1990) has shown that intraseasonal signals, and more specifically intra-monthly modes, exhibit considerable space-time complexity, with a wide range of periods, geographical regions of influence, and times of occurrence. Following Straus and Shukla (1981), Hayashi and Golder (1986), and Ghil and Mo (1991), two sources of intraseasonal phenomena have been considered: (1) geographically fixed anomalies, such as blocking or teleconnection patterns, and (2) transient wave modes (both travelling and standing) having broad spectral peaks. A common problem of intraseasonal variability simulation has been the underestimation of the amplitude of the low-frequency waves (Straus and Shukla, 1981). Such deficiencies can affect medium-range predictability because of the low-frequency tropical forcing by extratropical modes (Lau and Chang, 1992). In general, a dynamical approach to solve the model drawbacks requires the introduction of some improvements in either model physics, numerical model design or spatial resolution. Concerning resolution, some authors (Jones et al., 1997) have demonstrated specific improvements in climate GCMs by increasing horizontal and vertical resolution. An accurate assessment of the dependence of the model performance on horizontal resolution is a key issue for improving GCMs because of the need for much more computational resources at higher resolutions.

Sensitivity to horizontal resolution of global atmospheric numerical simulations has been studied since the earliest simulations with global models. Manabe et al. (1970) and Wellck et al. (1971) noted improvements with increased resolution. Miyakoda et al. (1971) showed that with finer-mesh models, better extended-range forecasts could be produced for the amplitudes of all of the waves even on the planetary scales, alleviating their underestimation. However, Manabe et al. (1978) showed that some aspects, such as low-level westerlies, can degrade with increased resolution. Baumhefner and Downey (1978) showed, by using numerical weather prediction (NWP) models, that not only poor simulation of the large scales can adversely affect short-term forecasts,

but also that increased resolution beyond a limit does not necessarily guarantee better accuracy. However, Chen et al. (1990) found that simulation of stationary eddies improves with increased resolution due to an enhancement of vorticity sources associated with tropical diabatic heating. More recently, Boer and Lazare (1988), Jarraud et al. (1988), Rind et al. (1991), Boville (1991), Kiehl and Williamson (1991), Boyle (1993), Chen and Tribbia (1993), Glecker and Taylor (1993), Sperber et al. (1994), Phillips et al. (1995), Stephenson and Royer (1995), Williamson et al. (1995), and Stephenson et al. (1998) have considered the problem with climatic versions of GCMs. Although many features of simulations vary monotonically with resolution, increasing resolution is not always a guarantee of overall improvement in the results. The lack of consistency between models suggests that physical parameterizations play a large role, and that different parameterizations may behave differently as the resolution is changed. A common and interesting result is that there often exists a limit beyond which increasing horizontal resolution does not meaningfully improve simulations, but instead might degrade them. Tibaldi et al. (1990) found that medium-resolution simulations prove to be better than low-resolution ones, and more or less equivalent in performance to higher resolution experiments. Boyle (1993) concluded that the zonal-mean diagnostic did not present a systematic improvement when the resolution increases beyond T42. Moreover, a tendency has appeared for the low-level westerlies to increase significantly with horizontal resolution (Held and Phillips, 1993). At sufficiently high horizontal resolution, GCMs will typically produce westerlies in the Northern Hemisphere winter that are much stronger than observed. To cope with this problem a solution that has been adopted in many GCMs is to include a drag on the zonal flow ascribed to topographically forced subgrid-scale gravity waves (Palmer et al., 1986; Boer and Lazare, 1988). Subgrid-scale gravity wave parameterization is strongly affected by horizontal resolution because in climate GCMs some of the largest differences between low (T21 spectral triangular truncation) resolution, medium (T42) and high (T106) resolution simulations can be associated with orography representation.

The possible improvement of simulated intrase-

asonal variability due to enhanced horizontal resolution is an important issue in current model development. We revisit the resolution issues discussed by in Déqué and Piedelievre (1995, hereafter DP) with the ARPEGE GCM simulations, who showed that the mean wintertime circulation over the Euro-Atlantic region improved only slightly with resolution. This study is primarily focused on assessing the ability to better reproduce the midlatitude intraseasonal variability over the Euro-Atlantic region by increasing horizontal resolution.

The paper is organised as follows. The GCM and data used are briefly described in Section 2. In order to demonstrate the model variability performance over the Euro-Atlantic region, a variability study is carried out on ECMWF analyses and on the simulations made with the ARPEGE GCM, and a comparison of results is performed and presented in Section 3. In Section 4, blocking behaviour is discussed. Finally, a brief summary and discussion conclude this paper.

2. Data sets and analysis procedures

2.1. Data sets

The study is based on four datasets consisting of gridded daily 500 hPa geopotential heights of ten December to February (sample size of 900 days) winters. They consist of the ECMWF analyses (December 1983 to February 1993), CEP henceforth, and three 10-year integrations of the ARPEGE (Action de Recherche, Petite Echelle, Grande Echelle, which means research project on small and large scale) GCM denoted by their spectral truncation numbers: T42, T106, and T63s. The ARPEGE GCM was adapted from a spectral NWP model for the simulation of the tropospheric and stratospheric climate. The basic climate versions are described in Déqué et al. (1994) (version 0) and DP (version 1). T42 and T106 spectral truncations have $2.8°$ and $1.125°$ longitudinal grid spacing, respectively. This spectral model also offers the possibility of locally varying horizontal resolution using the conformal mapping described in Courtier and Geleyn (1986). The T63s simulation has variable resolution with maximum horizontal resolution over the Mediterranean. From there its horizontal resolution diminishes attaining a minimum ($\cong$ T18) over the South Pacific (as can

be seen in Fig. 1 of DP, where all the experiments used here are described in more detail). Recently, this type of GCM has also been used at UCAR (University Corporation for Atmospheric Research) (Hardiker, 1997). Prescribed daily SSTs were linearly interpolated in time from observed monthly mean fields.

A space domain ranging from $90°W$ to $90°E$ and from $0°$ to $90°N$ has been selected. The Euro-Atlantic region has been chosen because the resolution is higher there for the variable horizontal resolution version. For practical purposes, T106 and T63s data ought to be projected on the T42 version grid, so that the domain comprises a grid with 65 longitude lines and 32 latitude lines.

2.2. Space-time spectral analysis

Hayashi (1982) presented a general method to study variability by using space-time Fourier spectral analysis. This method allows a partition to be made between standing and travelling wave variance. Such an analysis has been extensively applied to data generated by atmospheric models in Hayashi and Golder (1977), Vautard et al. (1988), and Hayashi and Golder (1993), among others, in an attempt to determine the characteristics, structure and energetics of transient atmospheric waves. This method is a simple approach based on the presumption of stationarity of the processes and the near Gaussian distribution of the data (Stephenson, 1997).

Space-time spectral analysis is applied along a latitude on a given longitude-time series $q(\lambda, t)$ which is cyclic in longitude (λ) and limited in time (t). Total space-time variance of any function $q(\lambda, t)$, with M spatial points and N observations, may be decomposed as

$$[\overline{q^2}] = [\bar{q}]^2 + [\bar{q}*^2] + \overline{[q]'^2} + \overline{[q'*^2]}$$
$$= A1 + A2 + A3 + A4 \tag{1}$$

where square brackets denote zonal average, the overbar denotes the time average, the asterisk the zonal deviation, and the prime, the time deviation. In this expansion each term may be associated with a different phenomenon. The first term represents the spatio-temporal mean, the second term (A2) represents the variance of climatological stationary waves (forced by transients, topography and heating contrasts), the third term (A3) represents the fluctuations of the zonal mean, and the

last term (A4) contains the variance of the combined space-time transients. When both zonal and time means are subtracted from the data, only the last term (transient waves) remains. The space-time variance of the transient eddies q'^* can be expressed (Hayashi, 1971) as

$$\sqrt{[q'^{*2}]} = \sum_{k=0}^{M/2} \sum_{m=-N/2}^{N/2} E_q(k, m) \qquad (2)$$

where $E_q(k, m)$ is the space-time Fourier spectrum. The spectrum represents the contribution to $\sqrt{[q'^{*2}]}$ from all the transients of wavenumber k and frequency ω ($\omega = 2\pi/m$), eastward (positive frequencies) and westward (negative frequencies). In practice, smoothed estimates of variance within a range of frequencies rather than for a single frequency are obtained due to the natural dispersion of variance over several frequencies because of the basically nonlinear character of the atmosphere, as well as the likely Doppler effect of zonal wind variations on zonally propagating waves.

In the present study, Pratt's (1976) one-sided formulation of space-time spectral analysis has been adopted. The sum of an eastward and a westward propagating wave of equal zonal wavenumber, frequency and amplitude may be considered as a standing oscillation with longitudinally fixed nodes and anti-nodes. The difference between the eastward and westward components is of more interest than their absolute magnitudes, when zonally propagating fluctuations are investigated. For this reason, it is more reasonable to present space-time spectra in terms of the one-sided spectral definitions. The total variance $T(k, \omega)$ is defined in Pratt (1976) by

$$T(k, \omega) = E_q(k, +\omega) + E_q(k, -\omega) = \tfrac{1}{2}\{P_\omega[C_k(t)]$$
$$+ P_\omega[S_k(t)]\}, \qquad (3)$$

which represents the sum of the eastward and westward contributions involved in (2), where $C_k(t)$ and $S_k(t)$ are the cosine and sine coefficients from a zonal Fourier analysis at time t and P_ω is the power spectrum. Propagating (PR) variance is defined as

$$PR(k, \omega) = |Q_\omega[C_k(t), S_k(t)]|, \qquad (4)$$

where $Q_\omega(C_k, S_k)$ is the quadrature spectrum (Chatfield, 1984). The propagating variance spectrum as defined in (4) is one-sided in frequency, and propagation direction can be determined from the algebraic sign of quadrature, i.e. if quadrature

is positive then variance is propagating zonally eastward, and the opposite for a negative quadrature. This represents the lower limit of the variance due to the propagating eddies (Hansen et al., 1989). A measure of standing (ST) wave activity is given by

$$ST(k, \omega)$$
$$= \sqrt{K_\omega^2[C_k(t), S_k(t)] + \tfrac{1}{4}\{P_\omega[C_k(t)] - P_\omega[S_k(t)]\}}, \qquad (5)$$

where $K_\omega(C_k, S_k)$ is the cospectrum. This may be interpreted as a coherent part of the space-time variance and describes the temporal variability of the amplitude of the standing eddies. Nevertheless, as mentioned in Hayashi (1977), there is no unique partition of the space-time power spectra because of the non-orthogonality of the standing and travelling wave parts. This non-orthogonality also introduces the possibility of correlation between the standing and the propagating parts. All of these problems suggests applying some caution when interpreting the results, although important general features may be extracted as was asserted by Hansen et al. (1989).

2.3. Complex principal component analysis

Principal component analysis (PCA) is a multivariate statistical method used to detect the maximum variance structure of a field. However, it is usually based on simultaneous correlations so that only standing perturbations or local instantaneous anomalies can be detected. To detect the presence of propagating phenomena and to characterise their structure, a generalised version of the common eigenvector analysis technique known as complex principal component analysis (CPCA) may be used. CPCA may be considered as a complement to the spectral analysis since it provides more information on the spatial structure of moving and standing transients, although it does not say much about scale separation. CPCA is accomplished by using a complex data set consisting on the original data augmented by their Hilbert transform. The later is computed as a time series having the same power spectrum as the original one but phase-shifted by 90° (Oppenheim and Schafer, 1975) to help produce empirical functions which depict the amplitude and phase variations in the data. The resulting amplitude-

phase functions can represent coherently propagating modes.

Two approaches to CPCA are commonly used. One considers either digital filtering or Fourier analysis to build the Hilbert transform, which is added as the imaginary part to the original data. The correlation or covariance matrix is then computed and its eigenvectors found (Barnett, 1983, 1985; Horel, 1984; Lanzante, 1996). An alternative approach uses the cross-spectral matrix integrated by frequency bands (Wallace and Dickinson, 1972; Vautard et al., 1988). Let us consider a data matrix W constituted by M variables and N samples which define the time series of an M-dimensional vector. If this $N \times M$ matrix is subjected to cross-spectrum analysis, for any frequency band we obtain B, the cross-spectrum matrix. The diagonal elements of this matrix are the spectral power estimates, and the off-diagonal elements are complex, the real and imaginary parts being the cospectrum and the quadrature spectrum respectively. We may express the original vector time series as a linear combination of the eigenvector e_l of the cross-spectrum matrix which is an eigen-solution of B. The complex eigenvectors depict the spatial wavelengths and relative amplitudes, and may be alternatively represented by the spatial amplitude and spatial phase functions. The associated coefficient time series, the complex principal components (CPC) are thus also complex (Trenberth and Shin, 1984). They may be depicted as temporal amplitude and phase functions and are obtained from $C = AE^*$, where E^* is the adjoint of the eigenvector matrix and the elements of A are given by

$$q_{mj} = 2 \sum_{k=1}^{N_0} d_{kj} \exp(ik2\pi n), \qquad (6)$$

$$a_{mj} = 2 \sum_{k=1}^{N_0} d_{kj} \exp(i\omega_k n),$$

d_{kj} being the Fourier transform of the original jth time series for the kth Fourier frequency and N_0 the maximum frequency number.

The (complex) eigenvectors are orthogonal

$$\sum_{j=1}^{M} e_{lj} e_{kj}^* = \lambda_l \delta_{lk}, \qquad (7)$$

where e_{lj} is the lth eigenvector coefficient for the jth variable which, when squared, gives a measure of the covariance with the jth variable, and λ_l represents the eigenvalue which is real and measures the

variance explained by the corresponding eigenvector. The CPCs are orthonormal at zero lag

$$\sum_{m=1}^{N} c_{ml} c_{mk}^* = \delta_{lk}. \qquad (8)$$

It is also possible to evaluate the periodic character of the principal components. The period of the lth component is estimated from

$$t_l = \frac{2\pi(N-1)}{z_{Nl} - z_{1l}}, \qquad (9)$$

Z_{ml} being the temporal phase of the lth CPC for the time step n. Finally, the phase propagation of the perturbations may be assessed by means of

$$p_l = \frac{-2\pi}{t_l} \frac{\nabla f_l}{\|\nabla f_l\|}, \qquad (10)$$

f_l being the spatial phase of the lth eigenvector.

3. Intraseasonal space-time variability

3.1. General features

Although the main emphasis of this paper is on intraseasonal variability, it is of interest to briefly discuss the time-mean behaviour of both the observed and simulated mean troposphere as revealed by the 500-hPa geopotential height. The time-mean geopotential height for every data set are shown in Fig. 1. Their general distribution matches quite well the time-mean field of the analyses. However, the model field is too zonal over Eurasia, particularly in the T106 version, in agreement with the increase of zonalization with model resolution stated by Tibaldi et al. (1997). The zonal variance of the 500 hPa geopotential height stationary waves (term A2) has a maximum at 55°N (Fig. 2a). The model tends to underestimate and shift southward the stationary wave zonal variability, especially north of 50°N, with T63s being the most realistic version. The time variance of the zonal mean (term A3) for the analyses (Fig. 2b) is an increasing function of latitude up to about 60°N, where it shows a local maximum, whereas local maxima are found in the model at 45°N–50°N. This is consistent with the southward shift of the storm tracks and precipitation over Europe found by DP. Every version underestimate this type of variance, with differences statistically significant at 95% (here and henceforth a univariate Student t-test has been
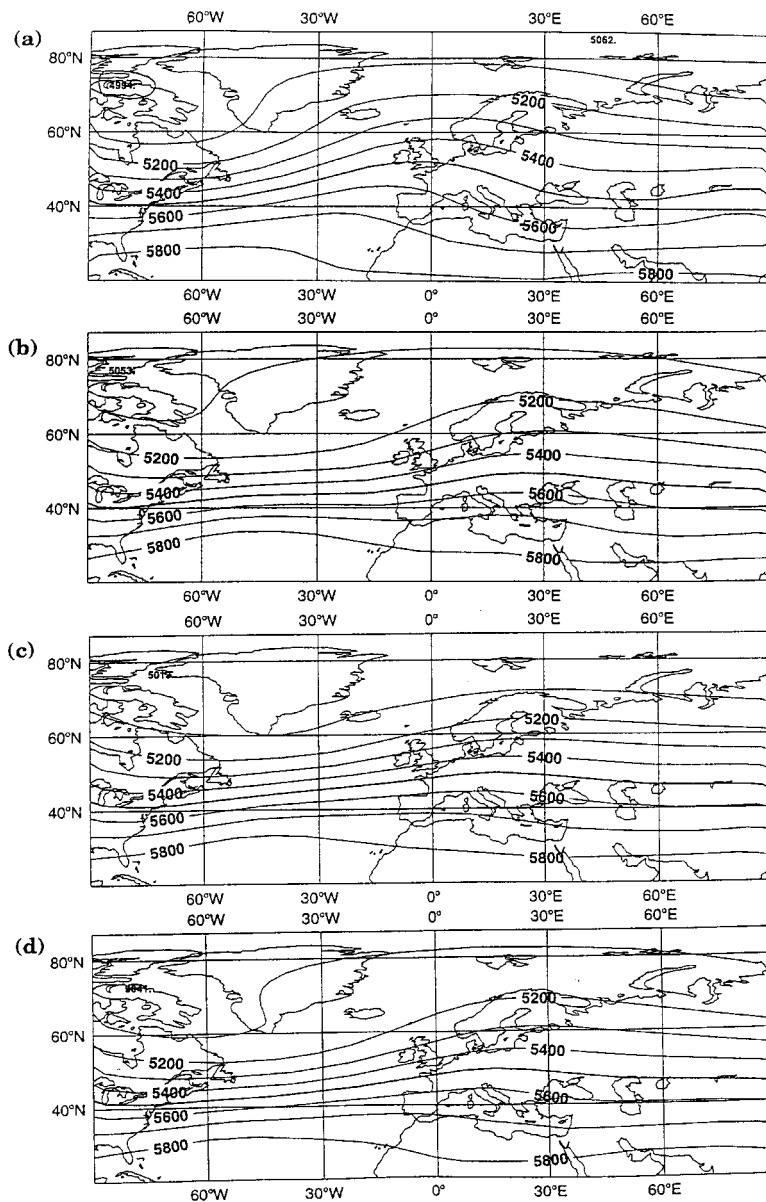
Fig. 1. Wintertime time-mean 500 hPa geopotential height for (a) the analyses and for the (b) T42, (c) T106, and (d) T63s ARPEGE GCM versions. Contour interval is 100 m.

used) south of 70°N, even though more variance embedding a slightly northward shift can be noticed in the T106 case. Such a feature denotes that the model has weak weather regime changes, which are slightly increased in the T106 version.

3.2. Spectral analysis

The space-time spectra of the 500 hPa daily geopotential height have been computed for individual seasons at every available latitude. Ten
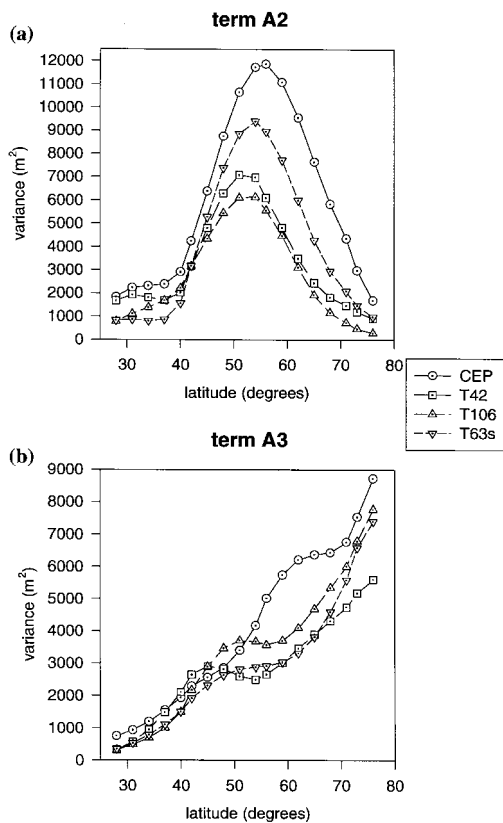
(a)

term A2

(b)

term A3

Fig. 2. (a) Latitudinal variation of the total variance of the 500 hPa geopotential height stationary waves for the analyses (circles, solid line) and for the T42 (squares, long-dashed line), T106 (up triangles, medium-dashed line), and T63s (down triangles, short-dashed line) ARPEGE GCM simulations. (b) Same as (a) but for time variance of the geopotential zonal mean.

samples, one for each year, of 90 consecutive days were taken. To estimate the spectra, the Fourier transform of the first 20 autocorrelation coefficients was used. The general results were not overly sensitive to the number of lags retained. A Hamming window was applied to the rough spectral values to obtain smooth spectral estimates. The ten spectra were averaged to obtain a mean estimate of the spectrum for every frequency-wavenumber pair. The spectra presented here have been cut off at $k = 7$ because we are interested in variability with scales greater than or equal to synoptic-scale transient eddies.

The total variance spectrum for the transient waves of the analysed data depicts decreasing
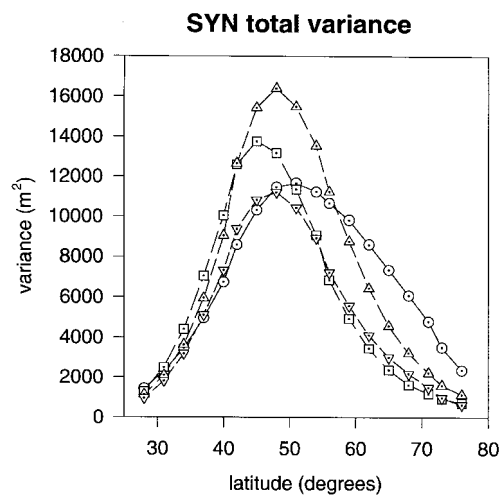
SYN total variance

Fig. 3. Latitudinal variation of the 500 hPa geopotential height total variance of the synoptic-scale medium-frequency transient eddies for the analyses (circles, solid line) and for the T42 (squares, long-dashed line), T106 (up triangles, medium-dashed line), and T63s (down triangles, short-dashed line) ARPEGE GCM simulations.

values with both frequency and wavenumber. For the latitude interval 35°N–65°N, a spectral peak is observed at $k = 2$–4 and $v = 0.2$–0.35 day^{-1} ($v = \omega/2\pi$). This spectral region, which corresponds to the synoptic-scale disturbances and will be denoted henceforth as SYN region, shows a maximum of variability at 50°N (Fig. 3) as in Straus and Shukla (1981). The model is in approximate agreement with the analyses, yet the SYN spectral region in Fig. 3 shows that total variance is overestimated south of 50°N (except for T63s) and underestimated north of 55°N (both statistically significant at 95%). Simulated maxima are too far south, as were the jet and the time-mean fields, which act as a waveguide for the synoptic-scale waves (Reynolds et al., 1996). The total variance of low-frequency planetary-scale waves (PLA henceforth) with frequency lower than 0.15 day^{-1} and $k = 1$, is in good agreement up to 50°N. A strong underestimation (statistically significant at 95%) occurs further north than 50°N, with values 50% less than in the analyses. The T106 version is somewhat improved.

The largest standing variance is found at both low-frequency and low wavenumber as was noted for standing ultralong waves by Fraedrich and Böttger (1978), and decreases approximately in a
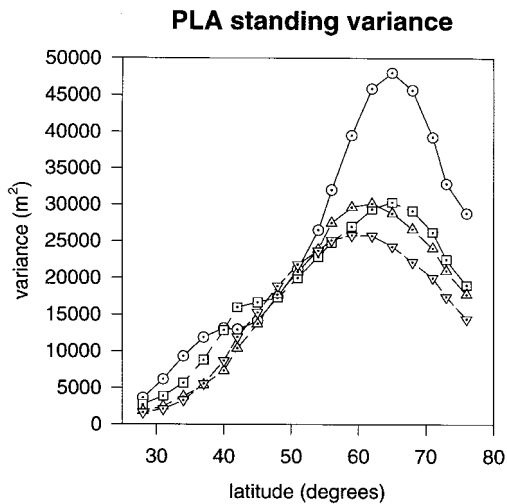
PLA standing variance

Fig. 4. Latitudinal variation of the standing variance of the 500 hPa geopotential height planetary-scale low-frequency transient eddies for the analyses (circles, solid line) and for the T42 (squares, long-dashed line), T106 (up triangles, medium-dashed line), and T63s (down triangles, short-dashed line) ARPEGE GCM simulations.

radial way from there. Figure 4 shows PLA standing variance increasing as a function of latitude attaining a maximum at 65°N, and decreasing further north. Such a latitudinal dependence similar to the PLA total variance (not shown) suggests the mainly standing character of planetary waves over the corresponding part of the hemisphere. There is also a maximum of standing variance at the SYN spectral region for the above mentioned latitudinal range, with a maximum between 55°N and 60°N. However, the SYN standing variance local maximum is associated with the increase of total variance. When the ratio between standing and total variance is computed, this region corresponds to a minimum, with values smaller than 0.3. Larger values of this ratio are found for wavenumbers close to $k = 1$, and for greater than $k = 5$ in low-frequencies. The latter may be produced by blocking events. The model PLA standing variance, as well as the total variance, is significatively underestimated north of 50°N and slightly south of 40°N (Fig. 4).

Propagative contributions may be either positive or negative. Values are positive (eastward propagation) for every wavenumber except for $k = 1$, where a portion of variance corresponding
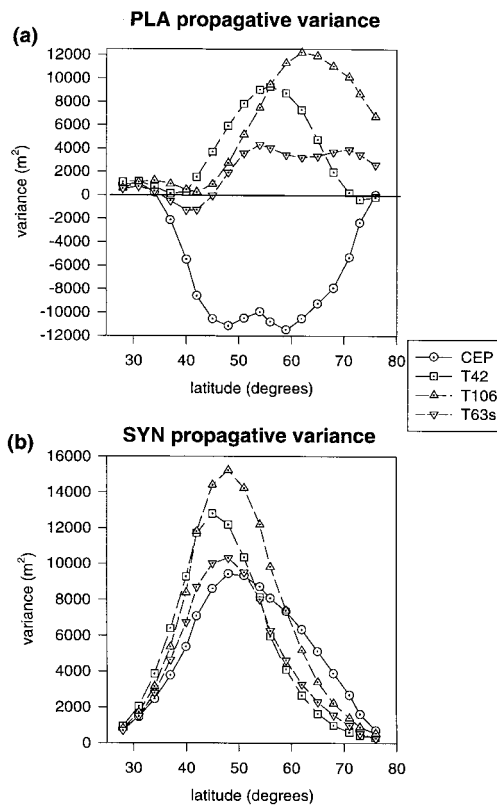

Fig. 5. (a) Latitudinal variation of the 500 hPa geopotential height propagative variance of the planetary-scale low-frequency transient eddies for the analyses (circles, solid line) and for the T42 (squares, long-dashed line), T106 (up triangles, medium-dashed line), and T63s (down triangles, short-dashed line) ARPEGE GCM simulations. (b) Same as (a) but for synoptic-scale, medium-frequency waves.

to low-frequency planetary westward travelling waves is found. North of 40°N low-frequency westward propagating variance is found with frequency ranging from 0.0–0.1 day^{-1} at 70°N to 0.0–0.2 day^{-1} at 40°N, which is the result of the superposition of a dominant westward component over an eastward component (Pratt and Wallace, 1976; Hayashi, 1982). South of 40°N, westward propagating waves frequency ranges from 0.05 to 0.3 day^{-1}, indicating the existence of another kind of westward propagating waves which encompass the 5-day period westward propagating mode southward of 50°N described by Madden (1978). Figure 5a shows the distribution of PLA propagat-

ive variance. Maxima of westward variance are found between 40°N and 60°N, agreeing with the results in Madden (1978) for 5-day (40°N) and 16-day (60°N) period waves, and tend to zero outside this latitude range. In Fig. 5(a) no evidence exists of westward travelling waves for the model, except perhaps at T63s. Maxima are found for eastward propagating variance north of 50°N. The differences, such as those in Fig. 4, are statistically significant at 95%. In contrast, both T106 and T63s exhibit some very low-frequency westward propagating variance in midlatitudes. The subtropical westward travelling variance with frequency higher than 0.05 day^{-1} is found in every version, especially in T63s (not shown). This is particularly important because this version, as mentioned above, reaches its highest resolution near 40°N (see Fig. 1 in DP95).

In Fig. 5(b), the maximum of SYN propagating variance at 50°N can be observed, being positive (eastward propagation) everywhere. An extended area with propagative-to-total variance ratios greater than 0.6 is found around the SYN region, showing that synoptic-scale perturbations are mostly eastward travelling. The three versions of the model resolve SYN propagative variance similar to that seen in the analyses. However, a clear overestimation of the maximum (the highest for T106) south of 50°N, as was also the case of the SYN total variance (Fig. 3), can be seen. The T106 version presents the greatest values in consistent agreement with both the higher zonality and SYN total variance.

Every spectrum has been computed again after removing the contribution of the annual cycle. The annual cycle was eliminated by subtracting the daily 10-year mean at each grid point. Prior to the subtraction, each mean time series was linearly filtered with a 30 points running mean in order to remove shorter-period oscillations. For the endpoints, asymmetric filters (Enting, 1989) were used. Results of the time-space spectral analysis were essentially the same, although an overall decrease in standing variance, as described in Hayashi and Golder (1986), was noted.

There is a distinct partition into low-frequency, which includes standing and westward travelling large-scale eddies, and medium-frequency, eastward propagating eddies associated with synoptic scales. The results presented here are in agreement with those found in previous studies on midlati-

tude intraseasonal variability (Willson, 1975; Pratt and Wallace, 1976; Vautard et al., 1988). The temporal scale separation used for CPCA relies on such a spectral gap. The model is found to have a tendency for less overall variability than the real atmosphere, mainly on the large scales and north of 50°N, and the increase in horizontal resolution does not solve the problem. Reynolds et al. (1996) have associated this deficiency to problems in the simulation of the tropical Madden-Julian oscillation. The model agrees better with the analyses for the synoptic scales than for the transient planetary scales, both for standing and propagating variances.

Kao and Lee (1977) suggested a possible mechanism for the undersimulation of low-frequency planetary westward travelling waves in a GCM. They found that the interaction between stationary waves and moving planetary waves tend to supply energy to the westward mode and extract energy from the eastward mode, so that the problem in the stationary wave variance may be due to the overestimation of the planetary eastward travelling wave variance. Alternatively, Hansen et al. (1989) showed that topography also plays an important role in the existence of westward planetary waves. They noted that these waves are more intense in the Northern Hemisphere than in the Southern Hemisphere. This fact could explain the subtle improvement obtained for westward planetary waves in the higher resolution versions, having a better representation of orography. The excess of SYN propagative variance may reflect a problem with the baroclinic energy conversion processes on synoptic scales (Pratt, 1979) which is reflected in a greater than normal storm track activity, as we shall show later. In fact, Johansson et al. (1993) noted that transient waves were too baroclinic in models (also for the ARPEGE GCM, A. Johansson, personal communication), especially for the synoptic-scale waves ($k = 3$–5).

3.3. Dominant space-time patterns

CPCA has been used to examine the dominant spatial and temporal modes of the intraseasonal variability in the Euro-Atlantic region. To reduce spatial dimensions, data were first submitted to a PCA and only the leading modes were retained. The arrangement of the input data matrix for the PCA corresponds to the S-mode (Richman, 1986),

i.e., columns contain grid point values and rows time realizations. The datasets here have more variables (2080) than time observations (900), so that the data matrix is rank-deficient and gives rise to a singular sample spatial covariance matrix. However, eigenvectors of this matrix can be found from those of the non-singular time covariance as shown in the Appendix.

Temporal anomalies have been computed by subtracting the day-to-day climatological means. The data have then been time filtered in order to separate the synoptic-scale activity from the low-frequency variability. The filters defined by Blackmon (1976) have been used: a low-pass filter passing periods longer than 10 days, which provides the low-frequency (LF) data, and a band-pass filter for periods ranging from 2 to 6 days, to isolate the medium-frequency (MF) or synoptic-scale data. The filtering process reduces the size of each winter sample from 90 to 74 days, and also changes serial correlation thereby changing the effective number of degrees of freedom. Data have been weighted by multiplying them by a normalised root cosine of the latitude, as done by Wallace and Hsu (1985), as points all over the grid are not homogeneously arranged, becoming closer northward. This is equivalent to weighting each grid point by the area it represents (Karl et al., 1982). It corrects also the biasing effect from the higher values of the geopotential variance in the northern part of the domain.

The number of modes to be retained after PCA was determined by examining the eigenvalue spectrum, following O'Lenic and Livezey (1988). In this way, the first 25 PC have been retained explaining near 80% of variance for MF data and more than 90% for LF data. Rinne and Järvenoja (1979) claimed that a few leading components of the geopotential field are able to explain the main features. Table 1 gives the percentage of variance associated with the components retained and with the three leading eigenvectors for each type of filtered data. Some degeneracy of the first two eigenvectors, mainly for MF data can be noted. An overestimation of 10% in the MF variance retained for the model also exists.

3.3.1. Synoptic-scale variability In Table 2, the main features of the first three complex principal components are given. It should be noted that the previous degeneracy of the first two PCA eigenvec-

Table 1. *Percentage of the total variance corresponding to the first 25 eigenvectors and each of the first three ones of the PCA performed on the MF (pass-band) and LF (low-frequency) data sets. The first column refers to the analyses and the other three to the three versions of the GCM.*

	CEP	T42	T106	T63s
MF				
Comp	75.3	84.5	84.5	86.7
e_1	12.3	19.3	17.9	18.9
e_2	11.3	18.8	17.4	18.0
e_3	5.7	5.6	6.0	5.8
LF				
Comp	96.5	97.3	97.7	97.8
e_1	18.5	20.3	21.0	23.3
e_2	15.3	17.8	17.5	14.4
e_3	9.3	11.2	13.8	14.0

Table 2. *Percentage of variance (Var) and mean period (τ_l) of the first three pairs of eigenvector-principal component of the CPCA performed on the MF and LF data sets obtained after PCA filtering. The standard deviation of τ_l is in parenthesis along with τ_l. CEP corresponds to the analyses and T42, T106, and T63s to the corresponding versions of the ARPEGE GCM.*

	Var	τ_l (days)	Var	τ_l (days)
CEP		MF		LF
e_1	22.6	4 (0)	16.7	52 (22)
e_2	10.2	4 (0)	13.1	40 (23)
e_3	5.9	4 (0)	10.6	31 (14)
T42		MF		LF
e_1	37.3	4 (0)	19.9	59 (25)
e_2	10.4	4 (0)	12.3	43 (20)
e_3	7.8	4 (0)	9.9	37 (17)
T106		MF		LF
e_1	34.7	4 (0)	21.7	47 (22)
e_2	11.5	4 (0)	15.9	35 (14)
e_3	8.5	4 (0)	10.2	28 (8)
T63s		MF		LF
e_1	36.1	4 (0)	20.9	55 (21)
e_2	10.6	4 (0)	14.1	37 (19)
e_3	8.8	4 (0)	11.1	30 (7)

tors for MF data has disappeared. Figure 6 illustrates the first MF eigenvector for the analyses (not degenerate at the 95% confidence level using
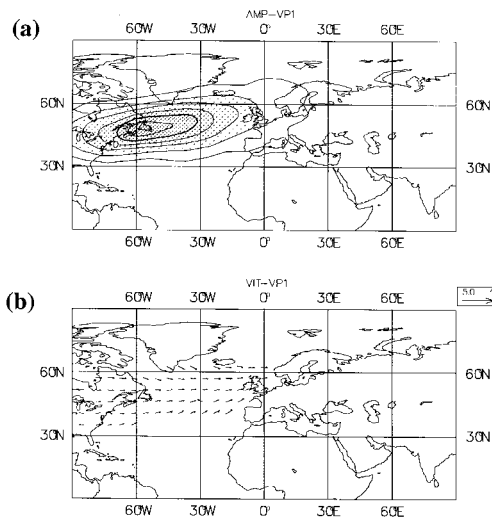
(a)

(b)

Fig. 6. (a) Amplitude and (b) inverse of the phase speed of the first MF (pass-band) complex eigenvector of the CEP 500 hPa geopotential height. The amplitude line interval is 10 m, the regions above 20 m are shaded, and the upper right corner box shows the maximum speed vector in 10^{-1} s/m.

Fig. 7. Amplitude of the second MF complex eigenvector of the (a) CEP and (b) T106 simulation 500 hPa geopotential height. The amplitude line interval is 10 m, the regions above 20 m are shaded.

the test described in Davis et al. (1991)). The amplitude plot shows a clear storm track related to the synoptic-scale baroclinic perturbations which travel zonally eastward over the Atlantic ocean, as shown by the inverse of the phase velocity displayed in Fig. 6(b)*. The maximum amplitude is northwards shifted over Europe. A similar eigenvector was also found by Davis et al. (1991) in a CPCA study of filtered SLP. The second eigenvector (Fig. 7a) shows a storm track maximum situated over the northern part of the Atlantic ocean between 60°W and 30°W. It is shown later to be associated with the northward deflection of the storm track by blocking events. The third one (not shown) is similar to the second in that it is northeastwards deflected, but the amplitude maximum is further east.

Pratt and Wallace (1976) recommended checking the dynamical consistency of modes before accepting them as physically significant. The amplitude of the principal components have been compared to the flow index defined by Liu (1994),

---

The inverse of the phase speed allows one to detect standing and slow propagating features, while also giving useful information about propagating modes.
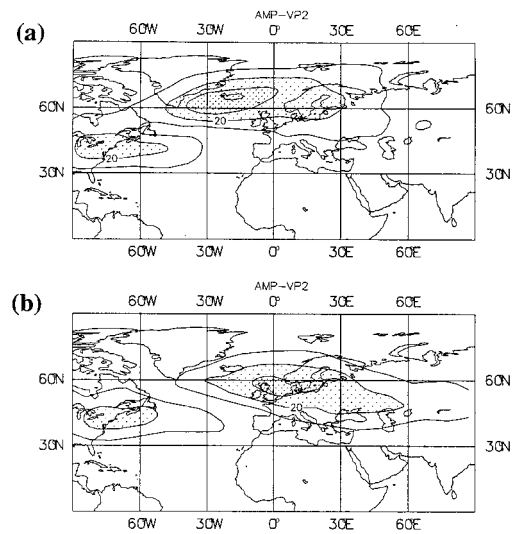
which we denote by ZA. This index, which is a zonal mean of the geopotential anomalies along a latitude line (typically 60°N), represents either a strong zonal flow situation when it is negative (over a threshold of 100 m, in absolute value), or blocked flow when positive. The largest values of the first component amplitude (not shown) are attained when ZA60 (ZA index at 60°N) is negative, that is, a close relationship may be established between the high amplitude events of the first eigenvector and the zonal flow. On the contrary, the second and third principal components are related to meridional flow events because the amplitude is high when ZA60 is positive. More precisely, they are related to intense ridges detected with positive values of the ZA45 index (ZA index at 45°N). In Fig. 8(a) the amplitude of the second principal component from the MF filtered CEP data is plotted against the low-frequency filtered ZA45 index and time. The largest amplitude values occur for the positive values of ZA. The first and second principal components seem to represent different phenomena (strong zonal and meridional flows, respectively). When displayed on the same plot as in Fig. 8b, the high values of their amplitudes lie mainly close to the respective axes. CPCA
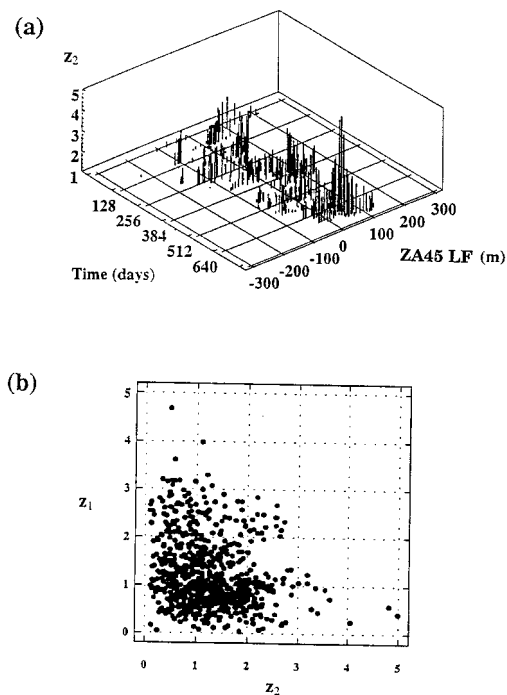
(a)

(b)

Fig. 8. (a) Three dimensional plot of the second MF complex principal component amplitude and the ZA45 index low-frequency filtered against time for the CEP 500 hPa geopotential height. (b) Amplitude of the first complex eigenvector of the CEP MF dataset against the amplitude of the second one for the CEP 500 hPa geopotential height.

(a)

(b)

(c)

Fig. 9. Amplitude of the first MF complex eigenvector of the (a) T42, (b) T106, and (c) T63s simulations 500 hPa geopotential height. The amplitude line interval is 10 m, the regions above 20 m are shaded.

appears to be able to separate storm track behaviour depending on the large-scale environment.

A similar first eigenvector as that of the analyses is observed for the model (also not degenerate), but it explains from 12% to 15% more variance than does the corresponding mode for the analyses, consistent with the excess of zonally propagating variance noted above. The leading T106 model eigenvector in Fig. 9b shows that the storm track penetrates further east over Europe. The amplitude fails to move northward over Europe compared to the analyses in Fig. 6a. These errors are present in each model version (Fig. 9a and c), but the maximum amplitude is smaller. The phase speeds are like those in the analyses (not shown). A second eigenvector similar to that in CEP is not present in any of the model results. Only the T106 version shows a second eigenvector for which the amplitude is shifted northwards in agreement
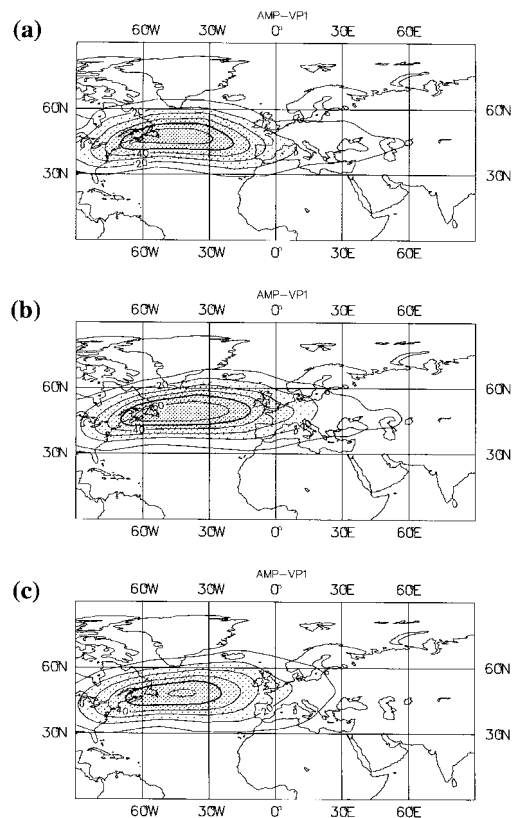
with the improved representation of low-frequency variability, although the shift is produced further east than in the analyses (Fig. 7b). Wallace and Hsu (1985) found that the quasi-stationary planetary waves are located further east during higher than during lower zonal index situations. If we accept at this point that the model is in a quasi-permanent high index state over the Atlantic when compared to the analyses, this may help to explain the eastward shift of both the storm tracks and the centres of low-frequency variability.

3.3.2. Synoptic-scale eddies and mean flow interaction. Results show that ARPEGE, like other models, exhibits a too intense zonal flow with greater than normal storm track activity (Tibaldi et al., 1990). It may be hypothesised that (a) orog-

raphic or heating contrast forcings are not well represented producing wrong stationary waves (Deland, 1964), and/or (b) transient forcing of the stationary waves is not correct (Stephenson and Held, 1993; Reynolds et al., 1996). The underestimation of the stationary wave amplitude and their poor spatial structure must be associated with the excess of zonal flow. On the other hand, modelled storm tracks are too far south, as are the time-mean fields. They also penetrate further east over Europe compared to those of the analyses. In fact, zonally oriented storm tracks are more frequent in the model as shown by the overestimation of the leading principal component variance (Table 2). So, the strong zonality of the mean zonal flow in the model may also in part be caused by excessive nonlinear transfer of momentum between synoptic scales and the zonal mean flow. A larger phase tilt of the anomalies in the MF real eigenvectors (not shown) occurs for the model than the corresponding eigenvectors of the analyses. The transient momentum fluxes can feedback on the mean flow. To diagnose this phenomenon, the E vectors (Hoskins et al., 1983; Trenberth, 1986) can be calculated. The horizontal components of the E vector are given by

$$E = \tfrac{1}{2}(\overline{v'^2} - \overline{u'^2}, \ -\overline{u'v'}) \cos \phi, \tag{11}$$

which indicates the shape and propagation of the transient eddies. A westerly E vector indicates meridionally elongated eddies with a group velocity to the east relative to the mean flow while an easterly E vector indicates zonally elongated eddies with westward group velocity relative to the mean flow. A divergent pattern indicates a westerly acceleration of the time-mean flow by the transient eddies by barotropic processes, while a convergent pattern indicates an easterly acceleration. Figure 10 shows the resultant E vectors from the first two MF eigenvectors (those associated with the zonal flow) for each data set. The divergence of the E vectors is also displayed in Fig. 10 as contour lines. E-vectors along the storm tracks in the model are divergent further east than in the analyses, suggesting that the eddies accelerate the mean flow all across the Atlantic, even if the initial forcing over the American coast is weaker (the model is too warm over the continent, reducing the thermal contrast with the ocean). The transient momentum fluxes in the model predominate on the equatorward side of the jet, E vectors on the

poleward side being negligible. This could lead to the southward shift of the storm tracks in the model because synoptic-scale eddies induce equatorward accelerations on the southern side of the storm track. T106 has again the more realistic features. As expected, eddies located over the region of maximum divergence have a higher tilt in the model than in the analyses, as indicated by the direction of the E vectors. This feature is even more outstanding at the eastern end of the storm track, implying too much northward momentum transfer by transient eddies in the model from regions south of 50°N (note that the meridional component of the vectors is stronger for the simulations).

3.3.3. Low-frequency variability. The two leading LF eigenvectors of the analysed data represent quasi-standing atmospheric modes and are degenerate. The first one (Fig. 11a) is reminiscent of the Western Atlantic pattern (Wallace and Gutzler, 1981). The slowly eastward propagating amplitude centre over Siberia might be explained by the propagation of planetary-scale anomalies described in Hansen and Sutera (1995) occurring during the decaying phase of large amplitude planetary wave events. A similar structure was described in Ghil and Mo (1991) as the superposition of an eastward propagating mode and a standing mode of 40–50 day period (note the agreement with the period of our mode in Table 2). The second one (not shown) corresponds to a low-frequency slowly eastward propagating pattern which amplifies over Europe, resembling the Eastern Atlantic teleconnection pattern. Such modes are often associated with intense negative anomalies over the Atlantic region during long periods of strong zonal flow. Evidence to support this is given by the fact that the highest values of the second principal component magnitude, shown in Fig. 12, are biased towards high negative values of ZA60. The third LF eigenvector, depicted in Fig. 13, represents a travelling westward wave-like mode, as shown by the inverse of the phase speed. Such a mode, which corresponds to the westward intramonthly mode described by Branstator (1987), Kushnir (1987), and Lanzante (1990), has a mean period of 30 days and may be associated with the planetary westward propagating waves that are severely misrepresented in the simulations.
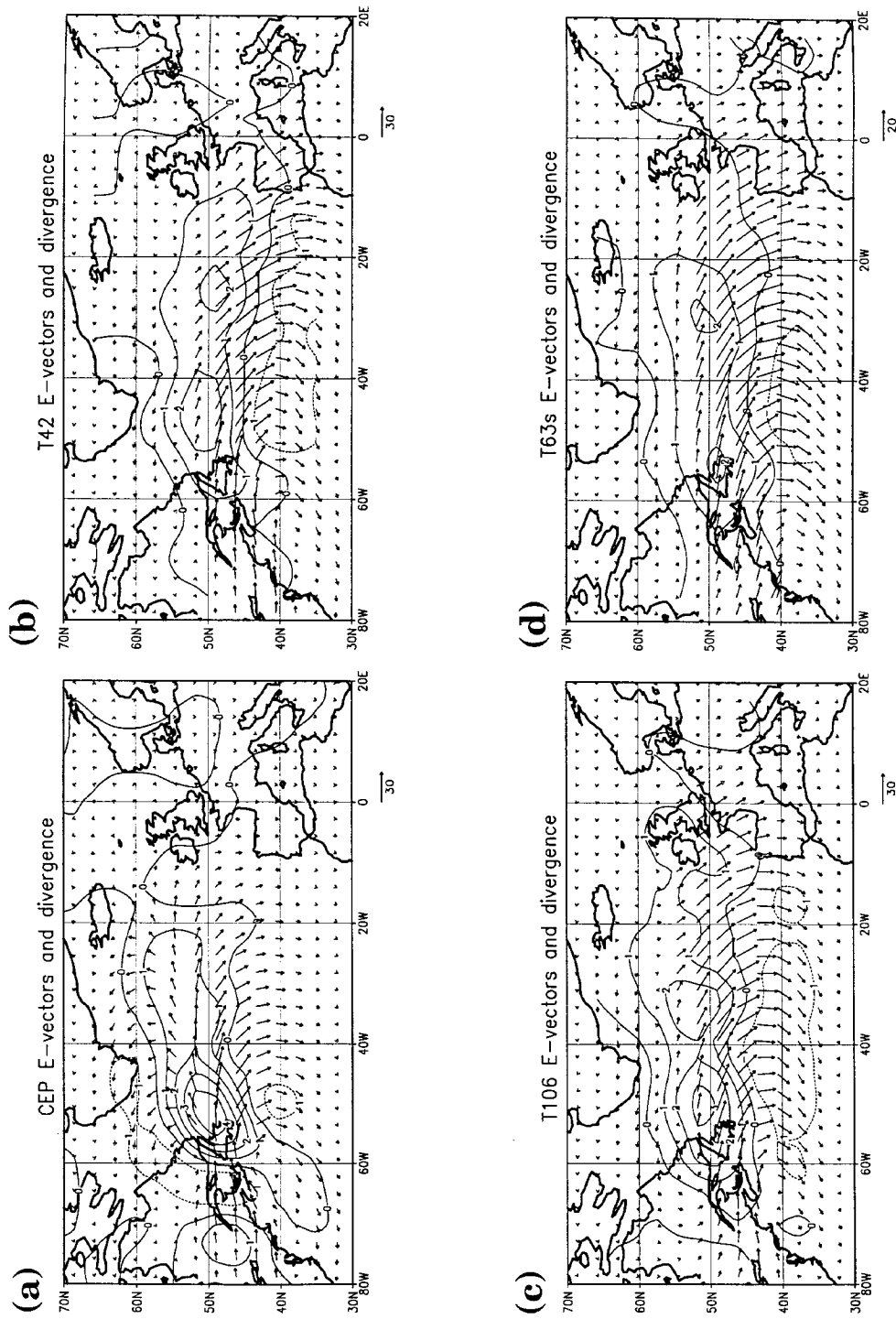
Fig. 10. **E** vector and its divergence computed with the two first MF real eigenvectors of (a) CEP, (b) T42, (c) T106, and (d) T63s. Contour interval is 10^{-5} m s^{-2} and the maximum vector is 100 m^2 s^{-2}.
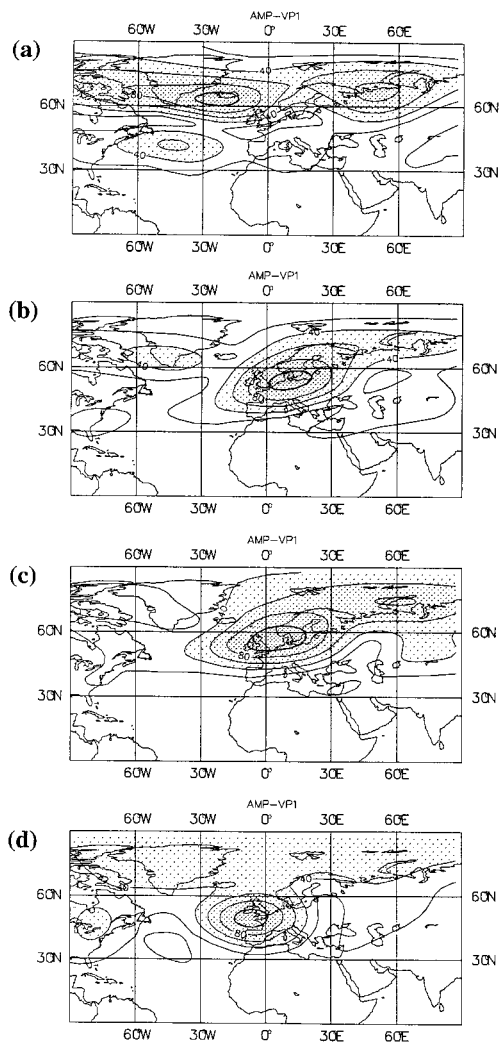
(a)

(b)

(c)

(d)

Fig. 11. Amplitude of the first LF (low-frequency) complex eigenvector of the (a) CEP, and (b) T42, (c) T106, and (d) T63s simulations, 500 hPa geopotential height. The amplitude line interval is 20 m, and the regions above 40 m are shaded.

The two leading eigenvectors of the model do not resemble closely the corresponding analysis eigenvectors. Furthermore, they are less degenerate (Table 2). The leading eigenvector agrees quite well in the three model versions (Fig. 11b, c, and d). This feature could be interpreted as a different dynamical positioning of the low-frequency variance in the model with regard to the
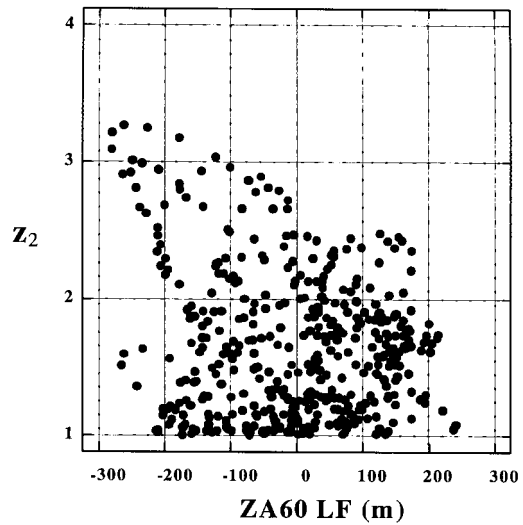

Fig. 12. Amplitude of the second LF complex eigenvector of the CEP 500 hPa geopotential height versus the low-frequency filtered ZA60 index. Note the high number of points in the upper left zone.
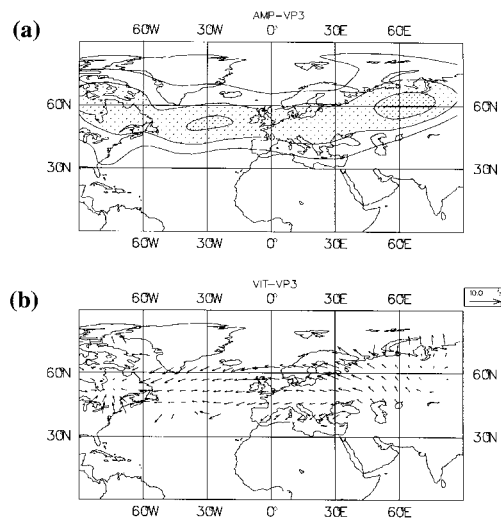

(a)

(b)

Fig. 13. (a) Amplitude and (b) inverse of the phase speed of the third LF (low-frequency) complex eigenvector of the CEP 500 hPa geopotential height. The amplitude line interval is 20 m, the regions above 40 m are shaded, and the upper right corner box shows the maximum speed vector in 10^{-1} s/m.

analyses. None of the model leading eigenvectors exhibit westward propagating features (Doblas-Reyes, 1994). On the contrary, a clear tendency to eastward propagating modes is observed. Lanzante (1990) suggests that the local index cycle-like variations that result from the oscillation of regional standing waves may excite the westward travelling waves in a feedback process. However, both low-frequency variability and location of the centres of action in the model are not realistic, and this could cause a hindrance to the correct simulation of the westward mode.

4. A specific phenomenon: midlatitude blocking

Blocking is an important manifestation of intraseasonal variability. It has been analysed in detail because of its known impact on European winter climate and because it is also undersimulated in some GCMs (Anderson, 1993; D'Andrea et al., 1996). An introductory general discussion about the potential of the use of blocking as a diagnostic tool for climate models can be found in Tibaldi (1993). Furthermore, Tibaldi et al. (1990) demonstrated that higher-resolution integrations better predicted the evolution of midlatitude anomaly fields during blocking episodes.

A blocking situation is recognised by a quasi-stationary positive height anomaly relative to a regional mean in which the normal eastward progression of migrating midlatitude weather systems is blocked or deflected. Blocking simulation is important for weather prediction since, in order to make relatively long-range forecasts, the model "climate" must be able of making blocks with the right amplitude and which persist (Tibaldi et al., 1994). In order to study blocking phenomena in long time series of atmospheric circulation data, objective procedures for identifying blocking events are required. A version of the Tibaldi and Molteni (1990) objective blocking index has been used in this study because it will allow us to make comparisons with previous analyses of blocking. The index, derived from the original Lejenäs-Økland index (Lejenäs and Økland, 1983), is based on testing the following geopotential height meridional gradients GHGS and GHGN at each

longitude λ

$$\text{GHGS}(\lambda) = \frac{Z(\phi_0, \lambda) - Z(\phi_s, \lambda)}{\phi_0 - \phi_s}$$

$$\text{GHGN}(\lambda) = \frac{Z(\phi_n, \lambda) - Z(\phi_0, \lambda)}{\phi_n - \phi_0} \tag{12}$$

where $\phi_n = 79.5°\text{N} + \Delta$, $\phi_0 = 60°\text{N} + \Delta$, $\phi_s = 40.5°\text{N} + \Delta$, $\Delta = m*2.8°$, $m = -1, 0, +1$, and $Z(\phi, \lambda)$ is the geopotential value at the grid point located at the latitude ϕ and longitude λ. A given longitude is locally defined as blocked for a specific day if, at least for one of the three values of Δ, the conditions $\text{GHGS} > 0$ and $GHGN < -5 \, \text{m/°lat}$ are fulfilled. The use of only a 10-year period to evaluate blocking frequency may cause sampling problems due to the presence of a strong inter-annual variability in the number of blocking events. Nevertheless, several authors (Anderson, 1993; D'Andrea et al., 1996) have successfully used 10-year periods to assess model blocking performance.

By applying this index to the four datasets, two main features stand out:

(1) Blocking frequency is highly underestimated, as has also been found for some other climate models (Sausen and Ponater, 1990; Kaas and Branstator, 1993; Huth, 1994).

(2) Maximum values are shifted eastward by about 20°-30° (especially for T42), as observed in previous studies (Tibaldi and Buzzi, 1983; Kaas and Branstator, 1993). This feature may be explained by considering that model blocking is formed mainly on a too intense zonal flow which shifts blocking highs eastward (Wallace and Hsu, 1985).

A clear eastward shift of the time-mean field is present in the simulations (Fig. 1). However, this might not be the case for blocking events. Since the index depends on the latitudes chosen for evaluating the meridional gradient, a way of removing the bias in blocking frequency due to the difference in time-mean states consists of subtracting the systematic error of the model:

$$Z_{\text{model}}(\phi, \lambda) = Z_{\text{model}}(\phi, \lambda) + \overline{Z_{\text{analysis}}(\phi, \lambda)} - \overline{Z_{\text{model}}(\phi, \lambda)}, \tag{13}$$

where the overbar means time averaging. The index has been applied to this corrected height field to give the blocking frequency shown in Fig. 14. Some of the eastward shift remains, but
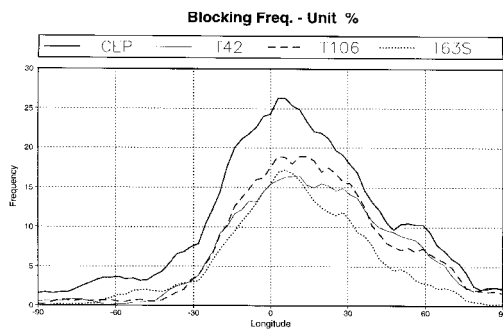
Fig. 14. Blocking frequency (in percentage) as a function of longitude for the analyses, CEP, (bold solid line), and for T42 (thin solid line), T106 (dashed line), and T63s (dotted line) ARPEGE GCM simulations. The model systematic error has been removed before applying the blocking index.

frequencies are closer to the analyses, especially for T106 for which the time-mean error is most apparent (Fig. 1). The increased blocking frequency for T106 is in agreement with the greater tendency of the corresponding storm track to drift more northeastward than in the other two versions. The secondary maximum observed in the analyses at 60°E is only reproduced by the T106 experiment. Model blocking frequencies are always less than those for the analyses.

As blocking shows a clear regional preference of formation, two main Northern Hemisphere blocking sectors have been considered for studying individual blocking. The corresponding longitudinal limits are 22.5°W–45°E for the Euro-Atlantic sector (EU) and 50°E–80°E for the Siberian sector (SIB). A sector is considered to be blocked if three or more adjacent grid points (spanning 9° longitude) over a latitude band are blocked according to the local index defined above. In addition, time-persistence is an important feature of blocking events. Thus, episodes were defined as events lasting more than four days. Nevertheless, some exceptions to this rule have been included as blocking episodes, following the work of D'Andrea et al. (1996), such as the threshold-edge episodes, i.e., those that intermittently may or may not fulfil the requirements of the index. Special events of this type are either the sequences of five blocked days with the third day being non-blocked or the sequences of six blocked days with the second or the fifth non-blocked day. To better distinguish

between persistent and non-persistent blocking, the first type will be referred to as *episodes* and the second type as *events*. In Table 3 the number of events, or blocked days, for the corrected fields is given. Values are underestimated in both sectors, T106 being the best version in the ATL sector and T42 in the SIB sector (maybe due to the greater eastward shift of blocking highs in this version). Simultaneous blocking events over both sectors also occur. A problem exists for the T63s version, both in absolute and relative (number of simultaneous to total blocked days ratio) frequency. The persistence of blocking over the Euro-Atlantic sector is well simulated, although it is undersimulated over the SIB sector. The definition of sectors allows one to compute the blocking signatures in which the eastward shift may also be appreciated (not shown). The SIB signature for the analyses corresponds to a wavenumber 3 wavetrain that resembles the negative phase of the Western Atlantic teleconnection pattern (Wallace and Gutzler, 1981) corresponding to an intense zonal flow over the Atlantic and a ridge over Eastern Europe. This pattern is also observed in the simulations, and is most realistic at T106 resolution.

The higher horizontal resolution gives slight increases in the blocking frequency, as in Tibaldi et al. (1997), in agreement with the better simulation of low-frequency distribution, despite the T106 simulation suffering from a stronger zonalization of the time-mean flow. Concerning this result, Grose and Hoskins (1979) have shown that mountains are a major source of planetary waves and Tibaldi and Buzzi (1983) pointed out the

Table 3. Number of blocked days, number of simultaneous blocked days (SIMUL), and ratio between the number of simultaneous and total number of blocked days (RSATL and RSSIB) over the Euro-Atlantic (ATL) and Siberian (SIB) sectors. CEP corresponds to the analyses and T42, T106, and T63s to the corresponding versions of the ARPEGE GCM.

	CEP	T42	T106	T63s
ATL	436	300	320	281
SIB	106	82	77	34
SIMUL	62	43	33	8
RSATL	0.14	0.14	0.10	0.03
RSSIB	0.58	0.52	0.43	0.24

close relationship between the onset and persistence of blocking and the planetary orography as a source of quasi-stationary planetary waves. Nakamura et al. (1997) showed the importance of these orographically generated waves for the Atlantic blocking. The amplitude of such waves is probably underestimated in the model, becoming one of the likely reasons for the underestimation of blocking frequency. The problem, however, of determining a dynamical cause for the underestimation of the blocking frequencies is complex since the orographic forcing is not essential to the production of all of the kinds of blocking patterns, as was shown in some no orography simulations (Tibaldi and Buzzi, 1983; Ambaum and Verkley, 1995).

Three processes of onset and maintenance of blocks can be considered to be the likely cause of the model errors for blocking simulation: (1) bifurcation of the zonal flow, (2) planetary wave-wave and mean zonal flow-wave interaction, and (3) synoptic-scale interaction with planetary waves. First, it seems plausible that local disturbances which establish a flow pattern such as the splitting of the jet, may resemble blocking, so that if they are in the right position (localised forcing may become important) they can lead to a proper blocking state (Bengtsson, 1979). This state could also have an attracting nature in the dynamical phase space. This process may be less active in the model as a result of the underestimation of the mean zonal flow variability in the 50°-70°N latitude band, the main area where blocking appears. In a different context, a blocking situation may be associated with anomalous amplitudes of the first few zonal wavenumber components (Da Silva and Lindzen, 1993). Hansen and Sutera (1984) have shown that planetary wave energy is greater during blocking events. As the model underestimates the amplitude of the stationary and transient planetary waves, the interaction between waves may not be well represented, with the predominance of the low-frequency planetary-scale propagative eastward mode playing an important role. Finally, there exists a close relationship between synoptic perturbations and blocking highs (Colucci, 1985; Shutts, 1986). Ji and Tibaldi (1983) emphasised the need for a deep cyclogenesis off the east coast of North America to trigger the Atlantic blocking. The feedback from eddies steered by the large-scale diffluent flow has been confirmed for the Northern Hemisphere by Vautard et al. (1988), Tsou and Smith (1990) and Lupo and Smith (1995). However, this process may not be adequately reproduced in the model because synoptic-scale transients penetrate too far east and south in the simulations.

5. Summary and discussion

The primary objective of the present study was to analyse wintertime intraseasonal variability over the North Atlantic basin and Europe. The European climate is strongly influenced by the intraseasonal perturbations over the Atlantic, in particular in winter (Plaut and Vautard, 1994). We have examined the variability in ten 90-day winters (1982/83 to 1992/93) of ECMWF operational 500 hPa height analyses. To test the GCM's ability to simulate intraseasonal variability at different model horizontal resolutions, three different 10-year simulations made with the ARPEGE GCM have been used. The highest resolution experiment (T106) is more zonal (having a too low stationary wave amplitude) than the two other runs, and also has too much synoptic-scale variability, consistent with an increase of zonality with resolution. The monotonic improvement of the stationary wave amplitude with increasing horizontal resolution observed by Chen and Tribbia (1993) is not observed here. However, higher resolution tends to give a better low-frequency variability representation as well as some more realistic blocking features and storm track spatial distribution.

Results show that ARPEGE, like many other models though in a greater extent, exhibits a too intense storm track activity over the North Atlantic, in agreement with the increase in zonality. The storm track penetrates further east over Europe. This point can be explained by considering the model to be in a quasi-permanent high index state over the Atlantic, which force the stationary planetary waves to be located further east than in the analyses (Wallace and Hsu, 1985). The storm track also fails to move northward over Europe compared to the analyses, but this is alleviated by increasing the resolution. An argument for explaining these drawbacks consists in considering that the increase in zonality is due

first to a problem in the long-term mean forcing which alters both stationary waves and storm tracks. Secondly, this produces a wrong forcing of the stationary waves by the synoptic-scale eddies. *E*-vectors have been computed to test this second hypothesis. Simulated eddies accelerate the mean flow all across the Atlantic, even when the land-sea lower level baroclinicity near the American east coast is weaker. Furthermore, synoptic-scale eddies induce equatorward accelerations on the southern side of the storm track which may explain their southward shift. There appears to be too much northward eddy momentum flux all across the Atlantic due to transient eddies from regions south of 50°N in the model.

Low-frequency planetary-scale variability is less well simulated than synoptic-scale variability, as was also noted by Huth (1994) for the UKMO model. Reduced low-frequency variance is a general feature of the three versions, mainly north of 50°N. This error is somewhat reduced by increasing the horizontal resolution of the model. The stretched T63 version degrades the simulation of planetary scales north of 45°N and performs worse than the other simulations. Spatial patterns of low-frequency intraseasonal variability are similar for the three versions of the model especially for the leading complex eigenvector, although they present very distinct features when compared with the analyses. In particular, the model does not exhibit westward travelling fluctuations, except south of 40°N for T106 and T63s. This suggests a dominance of the eastward over the westward low-frequency mode in midlatitudes described by Pratt and Wallace (1976). As a specific example of low-frequency phenomena, blocking has been studied. The analysis shows that blocking frequency is underestimated in the model, mainly due to model stationary wave errors as noted in Kaas and Branstator (1993). There exists an overall better performance for the T106 version, in agreement with its better low-frequency simulation. The underestimated blocking frequency in the model is consistent with the differences seen in the spatial distributions of the low-frequency complex eigenvectors. Increased probability of more zonal weather types in the model results in a different spatial distribution of low-frequency variance. Some dynamical reasons have been proposed to explain model blocking errors, namely, that the model does not correctly reproduce either

the instability of the zonal mean flow, the wave-wave interactions, and/or the between-scale transfer processes. Observations reveal that the eastern part of the storm track is diverted sometimes through developed ridges or blocking. Both blocking undersimulation and the lack of northeastward shift in the storm track simulated are closely related. The higher blocking frequency at T106 is consistent with a greater tendency for a northward shift of the corresponding storm tracks.

Pratt (1979), Eliasen and Laursen (1990), and Stephenson (1994) suggested that some differences between simulations may in part be attributable to variations in the horizontal diffusion and nonlinear transfers of wave energy. According to the results, it is not clear that merely increasing horizontal resolution will improve model performance, and careful tuning of the horizontal diffusion with resolution may be important because of the increasing ability of the model to resolve small-scale features. Finally, it may also be possible that the shortcomings of the present model in the tropics, i.e. excessive diabatic heating, excessive easterly zonal flow in the lower stratosphere (Cariolle et al., 1993), and a lack of intraseasonal variability, may cause some of the problems in the midlatitude tropospheric circulation. Some authors have outlined the tropical-extratropical connection (Anderson and Rosen, 1983) through the conservation of angular momentum, especially in the 20–50 day spectral band.

Consejería de Educación de la Comunidad de Madrid (Spain).

7. Appendix

The data matrix is said to be rank-deficient when its rank is greater than the minimum between columns (M) and rows (N). In this case the analysis cannot be completed in the S-mode, which diagonalizes the time-dispersion matrix. However, each eigenvector of the singular space-dispersion matrix may be obtained by the corresponding eigenvectors of the non-singular time-dispersion matrix. Let $B = (1/N)W^{T}W$ be the singular space-dispersion matrix ($M \times M$) obtained

from the (normalised) data matrix W, and let be the non-singular time-dispersion matrix ($N \times N$), where $N < M$. Let v_k denote the eigenvector of L associated with the eigenvalue λ_k

$$Lv_k = \lambda_k v_k, \tag{A.1}$$

Premultiplying by W^{T}

$$\frac{1}{N} W^{T}W(W^{T}Wv_k) = \lambda_k(W^{T}v_k), \tag{A.2}$$

$$B(W^{T}v_k) = \lambda_k(W^{T}v_k),$$

and hence $W^{T}v_k$ is an eigenvector of B associated with λ_k (if). If V is the eigenvector matrix of L, the eigenvector matrix of B, J, is given by

$$J = W^{T}V. \tag{A.3}$$

REFERENCES

Ambaum, M. H. P. and W. T. M. Verkley 1995. Orography in a contour dynamics model of large-scale atmospheric flow. *J. Atmos. Sci.* **52**, 2643–2662.

Anderson, J. L. 1993. The climatology of blocking in a numerical forecast model. *J. Climate* **6**, 1041–1056.

Anderson, J. R. and R. D. Rosen 1983. The latitude-height structure of 40–50 day variations in atmospheric angular momentum. *J. Atmos. Sci.* **40**, 1584–1591.

Barnett, T. P. 1983. Interaction of the monsoon and Pacific trade wind system at interannual time scales. Part I: The equatorial zone. *Mon. Wea. Rev.* **111**, 756–773.

Barnett, T. P. 1985. Variations in near global sea level pressure. *J. Atmos. Sci.* **42**, 478–501.

Baumhefner, D. and P. Downey 1978. Forecast intercomparisons from three numerical weather prediction models. *Mon. Wea. Rev.* **106**, 1245–1279.

Bengtsson, L. 1979. Review of theories for blocking. *Dynamical meteorology and numerical weather prediction*, ECMWF Seminar Proceedings, Reading, UK, 235–268.

Blackmon, M. L. 1976. A climatological spectral study of the 500 mb geopotential height of the Northern Hemisphere wintertime circulation. *J. Atmos. Sci.* **33**, 1607–1623.

Boer, G. J. and M. Lazare 1988. Some results concerning the effect of horizontal resolution and gravity wave drag on simulated climate. *J. Climate* **1**, 789–806.

Boville, B. A. 1991. Sensitivity of simulated climate to model resolution. *J. Climate* **4**, 469–485.

Boyle, J. S. 1993. Sensitivity of dynamical quantities to horizontal resolution for a climate simulation using the ECMWF (Cycle 33) model. *J. Climate* **6**, 796–815.

Branstator, G. 1987. A striking example of the atmosphere's leading traveling pattern. *J. Atmos. Sci.* **44**, 2310–2323.

Cariolle, D., M. Amodei, M. Déqué, J. F. Mahfouf, P. Simon and H. Teyssèdre 1993. A quasi-biennial oscillation signal in general circulation model simulations. *Science* **261**, 1313–1316.

Chatfield, C. 1984. *The analysis of time series. An introduction*, 3rd edition. Chapman and Hall, 286 pp., London.

Chen, T.-C. and J. J. Tribbia 1993. An effect of the model's horizontal resolution on stationary eddies simulated by the NCAR CCM1. *J. Climate* **6**, 1657–1664.

Chen, T.-C., J. Pfaendtner and J.-M. Chen 1990. The effect of horizontal resolution on systematic errors of the GLA forecast model, *Mon. Wea. Rev.* **118**, 1371–1378.

Colucci, S. J. 1985. Explosive cyclogenesis and large-scale circulation changes: Implications for atmospheric blocking. *J. Atmos. Sci.* **42**, 2701–2717.

Courtier, P. and J.-F. Geleyn 1988. A global numerical weather prediction model with variable resolution: Application to the shallow-water equations, *Quart. J. Roy. Meteor. Soc.* **114**, 1321–1346.

D'Andrea, F. et al. 1996. *Northern hemisphere atmospheric blocking as simulated by 15 atmospheric general circulation models in the period 1979–1988*. WCRP-96, WMO/TD-N°784, 68 pp.

Da Silva, A. M. and R. S. Lindzen 1993. On the establishment of stationary wave in the Northern Hemisphere winter. J. Atmos. Sci. **50**, 43–61.

Davis, J. M., F. L. Estis, P. Bloomfield and J. F. Monahan 1991. Complex principal component analysis of sea-level pressure over the eastern USA. *Int. J. Climatol.* **11**, 27–54.

Deland, R. J. 1964. Travelling planetary waves. *Tellus* **16**, 271–273.

Déqué, M. and J. P. Piedelievre 1995. High resolution

climate simulation over Europe. *Climate Dyn.* *11*, 321–339.

Déqué, M., C. Dreveton, A. Braun and D. Cariolle 1994. The ARPEGE/IFS atmosphere model: a contribution to the French comunity climate modelling, *Climate Dyn.* *10*, 249–266.

Doblas-Reyes, F. J. 1994. *Effet de la R ésolution Spatiale sur la Performance du Blocage du GCM ARPEGE-IFS.* GMGEC Technical note, no. 41, 58 pp (available from Météo-France, CNRM, 42 Av. Gaspard Coriolis, 31057 Toulouse Cedex, France).

Eliasen, E. and L. Laursen 1990. The effects of horizontal resolution and diffusion in a two-layer general circulation model with a zonally symmetric forcing. *Tellus* *42A*, 520–530.

Enting, I. G. 1989. Asymmetric filters for analyzing time series of atmospheric constituent data, *Tellus* *41A*, 109–114.

Fraedrich, K. and H. Böttger 1978. A wavenumber-frequency analysis of the 500 mb geopotential at 50°N. *J. Atmos. Sci.* *15*, 745–750.

Ghil, M. and K. Mo 1991. Intraseasonal oscillations in the global atmosphere. Part I: Northern hemisphere and tropics. *J. Atmos. Sci.* *48*, 752–779.

Glecker, P. J. and K. E. Taylor 1993. The effect of horizontal resolution on ocean surface fluxes in the ECMWF model. *Climate Dyn.* *9*, 17–32.

Grose, W. L. and B. J. Hoskins 1979. On the influence of orography on large-scale atmospheric flow. *J. Atmos. Sci.* *36*, 223–234.

Hansen, A. R. and A. Sutera 1984. A comparison of spectral energy and enstropy budgets of blocking versus nonblocking periods. *Tellus* *36A*, 52–63.

Hansen, A. R. and A. Sutera 1995. Large amplitude flow anomalies in Northern Hemisphere midlatitudes. *J. Atmos. Sci.* *52*, 2133–2151.

Hansen, A. R., A. Sutera and D. E. Venne 1989. An examination of midlatitude power spectra: evidence for standing variance and the signature of El Niño. *Tellus* *41A*, 371–384.

Hardiker, V. 1997. A global numerical weather prediction model with variable resolution. *Mon. Wea. Rev.* *125*, 59–73.

Hayashi, Y. 1971. A generalized method of resolving disturbances into progressive and retrogressive waves by space Fourier and time cross-spectral analysis, *J. Meteor. Soc. Japan* *49*, 125–128.

Hayashi, Y. 1977. On the coherence between progressive and retrogressive waves and a partition of space-time power spectra into standing and traveling parts. *J. Appl. Meteor.* *16*, 368–373.

Hayashi, Y. 1982. Space-time spectral analysis and its applications to atmospheric waves, *J. Meteor. Soc. Japan* *60*, 156–171.

Hayashi, Y. and D. G. Golder 1977. Space-time spectral analysis of mid-latitude disturbances appearing in a GFDL general circulation model, *J. Atmos. Sci.* *34*, 237–262.

Hayashi, Y. and D. G. Golder 1986. Tropical intrasea-

sonal oscillations appearing in a GFDL general circulation model and FGGE data. Part I: Phase propagation. *J. Atmos. Sci.* *43*, 3058–3067.

Hayashi, Y. and D. G. Golder 1993. Tropical 40–50 and 25–30 day oscillations appearing in realistic and idealized GFDL climate models and the ECMWF dataset. *J. Atmos. Sci.* *50*, 465–494.

Held, I. M. and P. J. Phillips 1993. Sensitivity of the eddy momentum flux to meridional resolution in atmospheric GCMs. *J. Climate* *6*, 499–507.

Horel, J. D. 1984. Complex principal component analysis: theory and examples. *J. Climate Appl. Meteor.* *23*, 1660–1673.

Hoskins, B. J., I. N. James and G. H. White 1983. The shape, propagation and mean-flow interaction of large-scale weather systems. *J. Atmos. Sci.* *40*, 1595–1612.

Huth, R. 1994. On the ability (or inability?) of GCMs to reproduce continental-scale circulation. In: *Contemporary climatology*, R. Brazdil and M. Kolar (eds.), 255–260. Masaryk Univ., Brno, Czech Rep.

Jarraud, M., A. J. Simmons and M. Kanamitsu 1988. Sensitivity of medium-range weather forecasts to the use of an envelope orography. *Quart. J. Roy. Meteor. Soc.* *114*, 989–1025.

Ji, L. R. and S. Tibaldi 1983. Numerical simulations of a case of blocking: the effects of orography and land-sea contrast. *Mon. Wea. Rev.* *111*, 2068–2086.

Jones, P. W., K. Hamilton and R. J. Wilson 1997. A very high resolution general circulation model simulation of the global circulation in austral summer. *J. Atmos. Sci.* *54*, 1107–1116.

Johansson, A., B. Reinhold and S. Saha 1993. Transient-induced climate drift. *J. Atmos. Sci.*, *50*, 1161–1172.

Kaas, E. and G. Branstator 1993. The relationship between a zonal index and blocking activity. *J. Atmos. Sci.* *50*, 3061–3077.

Kao, S. K. and H. N. Lee 1977. The nonlinear interactions and maintenance of the large-scale moving waves in the atmosphere. *J. Atmos. Sci.* *34*, 471–485.

Karl, T. R., A. J. Koscielny and H. F. Díaz 1982. Potential errors in the application of principal component (eigenvector) analysis to geophysical data. *J. Appl. Meteor.* *21*, 1183–1186.

Kiehl, J. T. and D. L. Williamson 1991. Dependence of cloud amount on horizontal resolution in the National Center for Atmospheric Research Community Climate Model. *J. Geophys. Res.* *96*, 10955–10980.

Kushnir, Y. 1987. Retrograding wintertime low-frequency disturbances over the North Pacific Ocean. *J. Atmos. Sci.* *44*, 2727–2742.

Lanzante, J. R. 1990. The leading modes of 10–30 day variability of the extratropics of the Northern Hemisphere during the cold season. *J. Atmos. Sci.* *47*, 2115–2140.

Lanzante, J. R. 1996. Lag relationships involving tropical sea surface temperatures. *J. Climate* *9*, 2568–2578.

Lau, K.-M. and M. J. Nath 1987. Frequency dependence of the structure and temporal development of win-

tertime tropospheric fluctuations — Comparison of a GCM simulation with observations. *Mon. Wea. Rev.* *115*, 251–271.

Lau, K.-M. and F. C. Chang 1992. Tropical intraseasonal oscillations and extended range forecasts in the NMC operation model. *J. Climate 5*, 1365–1378.

Lejenäs, H. and H. Økland 1983. Characteristics of Northern Hemisphere blocking as determined from a long time series of observational data. *Tellus 35A*, 350–362.

Liu, Q. 1994. On the definition and persistence of blocking. *Tellus*, *46A*, 286–298.

Lupo, A. R. and P. J. Smith 1995. Climatological features of blocking anticyclones in the Northern Hemisphere. *Tellus 47A*, 439–456.

Madden, R. A. 1978. Furtehr evidence of traveling planetary waves. *J. Atmos. Sci. 35*, 1605–1618.

Manabe, S., J. Smagorinsky, J. L. Holloway and H. M. Stone 1970. Simulated climatology of a general circulation model with a hydrologic cycle. III: Effects of increased horizontal computational resolution. *Mon. Wea. Rev. 98*, 175–212.

Manabe, S., G. Hahn and J. L. Holloway 1978. Climate simulations with GFDL spectral models of the atmosphere. Report of the *JOC study conference on climate models: performance, intercomparison and sensitivity studies.* GARP Publication Series 22, vol. 1, 41–94. WMO, Geneva.

Miyakoda, K., R. F. Strickler, C. J. Nappo, P. L. Baker and G. D. Hembree 1971. The effect of horizontal grid resolution in an atmospheric circulation model. *J. Atmos. Sci.*, *28*, 481–499.

Nakamura, H., M. Nakamura and J. L. Anderson 1997. The role of high- and low-frequency dynamics in blocking formation. *Mon. Wea. Rev. 125*, 2074–2093.

O'Lenic, E. A. and R. E. Livezey 1988. Practical considerations in the use of rotated principal component analysis (RPCA) in diagnostic studies of upper-air height fields. *Mon. Wea. Rev. 116*, 1682–1689.

Oppenheim, A. V. and R. W. Schafer 1975. *Digital signal processing.* Prentice-Hall, 585 pp.

Palmer, T. N., G. J. Shutts and R. Swinbank 1986. Alleviation of systematic westerly bias in general circulation and numerical weather prediction models through an orographic gravity wave drag parametrization. *Quart. J. Roy. Meteor. Soc. 112*, 1001–1039.

Phillips, T. J., L. C. Corsetti and S. L. Grotch 1995. The impact of horizontal resolution on moist processes in the ECMWF model. *Climate Dyn. 11*, 85–102.

Plaut, G. and R. Vautard 1994. Spells of low-frequency oscillations and weather regimes in the Northern Hemisphere. *J. Atmos. Sci. 51*, 210–236.

Ponater, M., W. König, R. Sausen and F. Sielmann 1994. Circulation regime fluctuations and their effect on intraseasonal variability in the ECHAM climate model. *Tellus 46A*, 265–285.

Pratt, R. W. 1976. The interpretation of space-time spectral quantities, *J. Atmos. Sci. 33*, 1060–1066.

Pratt, R. W. 1979. A space-time spectral comparison of the NCAR and GFDL general circulation models to the atmosphere, *J. Atmos. Sci. 36*, 1681–1691.

Pratt, R. W. and J. M. Wallace 1976. Zonal propagation characteristics of large-scale fluctuations in the mid-latitude troposphere, *J. Atmos. Sci. 33*, 1184–1194.

Reynolds, C., R. Gelaro and T. Murphree 1996. Observed and simulated Northern Hemisphere intraseasonal circulation anomalies and the influence of model bias. *Mon. Wea. Rev. 124*, 1100–1118.

Richman, M. B. 1986. Rotation of principal components. *J. Climatol. 6*, 293–335.

Rind, D., E.-W. Chiou, W. Chu, J. Larser, S. Oltmans, J. Lerner, M. P. McCormick and L. McMaster 1991. Positive water vapour feedback in climate models confirmed by satellite data. *Nature 349*, 500–503.

Rinne, J. and S. Järvenoja 1979. Truncation of the EOF series representing 500 mb heights. *Quart. J. Roy. Meteor. Soc. 105*, 885–897.

Sausen, R. and M. Ponater 1990. Reducing the initial drift of a GCM. *Contrib. Atm. Phys. 63*, 15–24.

Shutts, G. J. 1986. A case study of eddy forcing during an Atlantic blocking episode. In: *Advances in geophysics 29, Anomalous atmospheric flows and blocking*, R. Benzi, B. Saltzman and A. C. Wiin-Nielsen (eds.), 135–161. Academic Press, New York.

Sperber, K. R., S. Hameed, G. L. Potter and J. S. Boyle 1994. Simulation of the northern summer monsoon in the ECMWF model: sensitivity to horizontal resolution. *Mon. Wea. Rev. 122*, 2461–2481.

Stephenson, D. B. 1994. The impact of changing the horizontal diffusion scheme on the northern winter climatology of a general circulation model. *Quart. J. R. Meteor. Soc. 120*, 211–226.

Stephenson, D. B. 1997. The choice of metric in the correlation of spatial climate/weather maps and the advantages of using the Mahalanobis metric when making predictions, *Tellus 49A*, 513–527.

Stephenson, D. B. and I. M. Held 1993. GCM response of northern winter stationary waves and storm-tracks to increasing amounts of carbon dioxide. *J. Climate 6*, 1859–1870.

Stephenson, D. B. and J. F. Royer 1995. GCM simulation of the Southern Oscillation and its dependence on the model horizontal resolution. *Climate Dyn. 11*, 115–128.

Stephenson, D. B., F. Chauvin and J. F. Royer 1998. Simulation of the Asian summer monsoon and its dependence on model horizontal resolution. *J. Meteor. Soc. Japan 76*, 237–265.

Straus, D. M. and J. Shukla 1981. Space-time spectral structure of a GLAS general circulation model and a comparison with observations. *J. Atmos. Sci. 38*, 902–917.

Tibaldi, S. 1993. Low-frequency variability and blocking as diagnostic tools for global change models. In: *Prediction of interannual climate variations*, J. Shukla (ed.). NATO-ASI Series, *6*, Springer, Berlin, 173–182.

Tibaldi, S. and A. Buzzi 1983. Effects of orography on Mediterranean lee cyclogenesis and its relationship to European blocking. *Tellus 35A*, 269–286.

Tibaldi, S. and F. Molteni 1990. On the operational predictability of blocking. *Tellus* **42A**, 343–365.

Tibaldi, S., T. Palmer, C. Brankovic and U. Cubasch 1990. Extended-range predictions with ECMWF models: Influence of horizontal resolution on systematic error and forecast skill. *Quart. J. Roy. Meteor. Soc.* **116**, 835–866.

Tibaldi, S., P. Ruti, E. Tosi and M. Maruca 1994. Northern and Southern Hemisphere seasonal variability of blocking frequency and predictability. *Mon. Wea. Rev.* **122**, 1971–2003.

Tibaldi, S., F. D'Andrea, E. Tosi and E. Roeckner 1997. Climatology of Northern Hemisphere blocking in the ECHAM model. *Climate Dyn.* **13**, 649–666.

Trenberth, K. E. 1986. An assessment of the impact of transient eddies on the zonal flow during a blocking episode using localized Eliassen–Palm flux diagnostics. *J. Atmos. Sci.* **43**, 2070–2087.

Trenberth, K. E. and W.-T. K. Shin 1984. Quasi-biennial fluctuations in sea level pressures over the Northern Hemisphere. *Mon. Wea. Rev.* **112**, 761–777.

Tsou, C.-H. and P. J. Smith 1990. The role of synoptic planetary-scale interactions during the development of a blocking anticyclone. *Tellus* **42A**, 174–193.

Vautard, R., B. Legras and M. Déqué 1988. On the source of midlatitude low-frequency variability. Part I: A statistical approach to persistence, *J. Atmos. Sci.* **45**, 2811–2843.

Verkeley, W. T. M. 1990. Modons with uniform absolute vorticity. *J. Atmos. Sci.* **47,** 727–745.

Wallace, J. M. and R. E. Dickinson 1972. Empirical orthogonal representation of time series in the frequency domain. Part I: Theoretical considerations. *J. Appl. Meteor.* **11**, 887–892.

Wallace, J. M. and D. S. Gutzler 1981. Teleconnections in the geopotential height field during the northern hemisphere winter. *Mon. Wea. Rev.* **109**, 784–812.

Wallace, J. M. and H.-H. Hsu 1985. Another look at the index cycle. *Tellus* **37A**, 478–486.

Wellck, R. E., A. Kasahara, W. M. Washington and G. DeSanto 1971. Effect of horizontal resolution in finite-difference model of the general circulation. *Mon. Wea. Rev.* **99**, 673–683.

Williamson, D. L., J. T. Kiehl and J. J. Hack 1995. Climate sensitivity of the NCAR community climate model (CCM2) to horizontal resolution. *Climate Dyn.* **11**, 377–397.

Willson, M. A. G. 1975. A wavenumber-frequency analysis of large-scale tropospheric motions in the extratropical Northern Hemisphere. *J. Atmos. Sci.* **32**, 478–488.